Tailoring Hydrodynamics of Non-wetting Droplets with Nano-engineered Surfaces

by

Hyuk-Min Kwon

B.S., Mechanical Engineering, Seoul National University (2007)
M.S., Mechanical Engineering, Stanford University (2009)

Submitted to the Department of Mechanical Engineering
in partial fulfillment of the requirements for the degree of

Doctor of Philosophy in Mechanical Engineering

at the

MASSACHUSETTS INSTITUTE OF TECHNOLOGY

September 2013

Author .....
Department of Mechanical Engineering
August 16, 2013

Certified by .....
Kripa K. Varanasi
Associate Professor
Thesis Supervisor

Accepted by .....
David E. Hardt
Chairman, Department Committee on Graduate Theses

Tailoring Hydrodynamics of Non-wetting Droplets with Nano-engineered Surfaces

by

Hyuk-Min Kwon

Submitted to the Department of Mechanical Engineering
on August 16, 2013, in partial fulfillment of the
requirements for the degree of
Doctor of Philosophy in Mechanical Engineering

Abstract

Considering that contacts between liquid and solid are ubiquitous in almost all energy processes, including steam turbines, oil pumping, condensers and boilers, the efficiency of energy transportation can be maximized such that the liquid-solid interaction is optimized. Texture based super-hydrophobicity, also known as the Lotus effect, has been one of the most extensively studied topics in the last decade. Many of the recent studies have focused on how textures induce more water repellency, and how these textures can be manufactured with different methods and materials. However, few studies have shown how these surfaces benefit the real energy processes in which the interaction between liquid droplets and solid surfaces is vigorous and influences the energy transfer performances. This work focuses on altering the hydrodynamics of droplets with nano-engineered surfaces such that it enables a variety of energy transport processes to achieve better efficiency.

Firstly, the wetting transition on textured super-hydrophobic surfaces is explored. The careful investigation of Cassie-Baxter to Wenzel transition of a pendant drop during the deposition explains that the rapid deceleration-induced water hammer pressure causes the transition. This new transition mechanism for large droplets enables a new wetting transition phase diagram with a previously known Laplace mechanism that explains the small drop transition.

Another class of non-wetting droplet, the Leidenfrost drop, is studied with textured super-wetting surfaces. The liquid drop loses its contact to the solid by its own vapor, created by a large superheat from the solid. The Leidenfrost effect is undesirable in cooling applications as the vapor layer acts as a barrier for heat transfer. Here, it has been studied that how textured super-hydrophilic surfaces induce droplets to wet at higher superheat via capillary wicking compare to smooth surfaces. A physical model based on scaling is developed to predict the Leidenfrost drop on single length scale textures, and validated by the experiments. Additionally, the physical mechanism suggests that hierarchical textures have a higher Leidenfrost temperature compared to single-length-scale textures, confirmed experimentally.

Lastly, the recently discovered rare-earth oxide ceramics are studied, which ensures the benefits of water repellency under harsh conditions such as high temperature and abrasive

wear. Texturing of the rare-earth oxide ceramic is explored by the laser ablation technique. Unique micro- and nano-scale hierarchical textures are created, enhancing the water repellency, resulting in the super-hydrophobic rare-earth ceramic.

Thesis Supervisor: Kripa K. Varanasi
Title: Associate Professor

Acknowledgments

First, I would like to thank my advisor, Prof. Kripa Varanasi, who supported me with wise advice. I greatly admire his passion toward researches in surface engineering.

I am also thankful for the opportunity to work with Prof. Jacy Bird throughout the course of my research. His smart and discerning ideas were crucial to accomplish this work. I would also like to thank Dr. Rajeev Dhiman, and Dr. Gisele Azimi for the collaborative works on the reduction of the contact time, and the hydrophobic rare-earth oxide ceramics, respectively. I also greatly benefited from working along side Adam Paxson, whose help for completing the wetting transition experiments as well as setting up the laboratory equipment was invaluable. I would also like to thank the members of the Varanasi group members for their help in and out of the lab.

I extend my thanks to my thesis committee members, Prof. Jacopo Buongiorno and Prof. John Bush, and my previous advisor, Prof. Ho-Young Kim. My research as well as my professional development has greatly benefited from my interaction with them.

Finally, I am forever grateful to my family, my father, mother, and brother, for their constant love and encouragement, which made all the challenges of the completing my graduate study, and doctoral degree significantly easier.

Contents

Chapter 1

Introduction

As concern about limited natural resources and their environmental impact grow, engineers have focused on new energy conversion systems. However, there is a great potential to reduce resource consumption and improve operational efficiency of the existing systems. One of the most promising tools to do this is interfacial engineering, which alters the interaction between solid and liquid. This is crucial because the energy efficiency of many energy systems, including consumer electronics to power plants, depends on the energy exchange rate between liquid and solid. To pursue better transfer efficiency, liquid-solid interactions need to be curbed for some processes, and promoted for others. It has been shown that solid surfaces can be mechanically and chemically tailored to have better liquid repellency or affinity, known as super-hydrophobic and super-hydrophilic surfaces, respectively [1]. However, before these techniques are applied to various engineering applications, the fundamental mechanisms of how liquids interact with those engineered surfaces have to be satisfactorily studied. The goal of this thesis is to explain the hydrodynamics of droplet deformation on both textured non-wetting surfaces and the levitation of Leidenfrost droplets on textured super-wetting surfaces.

The first part of the thesis is mainly mechanisms of droplet dynamics on micro/nano texture based super-hydrophobic surfaces. There are two topics, deceleration-induced wetting transition from Cassie-Baxter to Wenzel. The next part discusses how textured super-wetting surfaces diminish the Leidenfrost effect, resulting in wetting of a liquid droplet to the solid at an elevated temperature. Lastly, the suitably controlled laser ablation is

shown to texture newly found hydrophobic rare-earth metal oxide ceramics, resulting in super-hydrophobic rare-earth oxides that are robust under harsh conditions, such as high temperature and abrasive wear.

1.1 Wetting transition of sessile droplets on textured super-hydrophobic surfaces

In Chapter 2, the wetting transition of droplets from Cassie-Baxter state to Wenzel state is discussed. A new mechanism, based on rapid deceleration of wetting transition from Cassie-Baxter to Wenzel state of sessile drops is studied, and a theoretically constructed regime map shows that both large and small droplets can transition to the wetted state due to the deceleration and previously known Laplace mechanism, respectively.

The most part of the Chapter 2 was published as Kwon, H., Paxson, A. T., Varanasi, K. K., Patankar, N. "Rapid deceleration driven wetting transition between hydrophobic states on rough surfaces." *Physical Review Letters* 106 (2011) 036102.

1.2 Prediction of the Leidenfrost drops on textured super-wetting surfaces

The solid roughness makes the hydrophilic solid more wettable by either decreasing the contact angle or adsorbing liquid through textures by capillarity, and by both ways at the same time, which can help liquid drops on hot surfaces to be wetted against a vapor layer, thereby diminishing Leidenfrost effect [3]. In Chapter 3, the critical temperature that separates wetting and non-wetting Leidenfrost states on fabricate micro-post arrays with different spacings was measured. Then, the result is rationalized with a proposed model that balances vapor pressure and capillary pressure, both of which depend on the design of texture. The increase in the Leidenfrost critical temperature which is demonstrated here with surface texture has the potential to increase the operational range and efficiency of these thermal hydraulic processes.

The most part of the Chapter 3 is to be published as Kwon, H., Bird, J. C., Varanasi, K. K. "Increasing Leidenfrost point using micro-nano hierarchical surface structures" *under review*.

1.3 Textured super-hydrophobic rare earth oxide ceramic

Recently, the hydrophobicity of rare-earth oxide ceramics has been thoroughly studied [4], and the robust hydrophobic ceramics opens many possibilities for hydrophobic coatings in extreme conditions to have various industrial applications. As known, suitable texturing of those hydrophobic ceramics will enhance the non-wetting property. In Chapter 4, laser ablation technique is applied to produce micro/nano hierarchical surface textures. It has been explored that the laser parameters that create surface textures and the mechanism of the texture formation. Also, the non-wetting characteristics of the textured super-hydrophobic ceramic is elaborated.

The most part of the Chapter 4 is to be published as Kwon, H., Azimi, G., Varanasi, K. K. "Textured super-hydrophobic rare-earth oxide surfaces by laser ablation" *in preparation*.

Chapter 2

Wetting Transition on Micro-textured Superhydrophobic Surfaces

Properly incorporated surface textures in micro/nano scale enable extreme water drop repellency by achieving the Cassie-Baxter state [5], in which liquid wets only on the upper part of surface textures, leaving the most part of it exposed to air. In contrast, a droplet penetrates through, completely wetting the surface features, known as Wenzel state [6]. Cassie-Baxter droplets have high mobility and repellency. However, when they transition to the Wenzel state, the surface loses the benefits of low hysteresis and high mobility. Therefore, the challenge is to understand what causes the Cassie-Baxter state to change into the Wenzel state [1].

2.1 Wetting transition of sessile droplets on textured superhydrophobic surface

For a sessile drop in the Cassie-Baxter state, liquid-air interface hangs between pillars in the Cassie-Baxter state. The interface is curved due to the pressure difference across it [7, 8, 9], and the amount of pressure difference is the capillary pressure, which is determined by the Young-Lapalce equation,

$$\Delta P_{cap} = \gamma\kappa \tag{2.1}$$

where γ is the surface tension of liquid, and κ is the curvature of a liquid-air interface. The Cassie-Baxter state is maintained when the pressure across the curvature of an interface can balance with the externally applied pressure. As any externally driven pressure exceeds the maximum possible capillary pressure across the interface that are pinned at the textures, here referred as the anti-wetting pressure, $\Delta P_{anti-wet}$, the interface impales through the textures and the drop transitions into the Wenzel state.

The maximum possible anti-wetting pressure is determined by two mechanisms, reported as de-pinning and sag [10]. The transition by the de-pinning mechanism occurs if the hanging interface cannot remain pinned at the pillar tops, set by the maximum possible contact angle, which is the advancing contact angle that can be maintained by the pinned interface at the textures. Then, it proceeds downward along the sidewalls of textures and fully wets [11, 12]. Even when a liquid-air interface can remain pinned at the pillar tops, transition to the Wenzel state begins when the sag in the curved liquid-air interface touches the bottom of the roughness groove [7, 9].

Any externally driven pressure, ΔP_{wet}, can cause the transition of Cassie-Baxter state drops into the Wenzel state when it exceeds the anti-wetting pressure, $\Delta P_{anti-wet}$. For a relatively small sessile drop, it is the pressure across the surface of the drop, often called the Laplace pressure, ΔP_{lap}, given as

$$\Delta P_{lap} = \frac{\gamma}{R} \tag{2.2}$$

where R is the radius of a drop. Thus, the smaller drop has the larger Laplace pressure, thereby more readily transiting to the Wenzel state.

2.2 Rapid deceleration driven wetting transition during pendant drop deposition

A transition into Wenzel state droplets was reported, and the gravity was implicated for the cause of the transition by Yoshimitsu et al. [13]. However, the gravity-induced transition is unclear because the water droplets used in their experiments were 1–12 mg, where the

gravity is not expected to play a dominant role. It is the capillarity that is dominant in the wetting problems on textured super-hydrophobic surfaces. The gravity is expected to be comparable to the capillarity as the Bond number, $Bo = \frac{\rho g L_c}{\gamma}$, scales to the unity at which the characteristic length is known as the capillary length, $\ell_c = \sqrt{\gamma/\rho g}$ where ρ is the density of a fluid. The weight of a water drop whose radius is the capillary length at room temperature, $\ell_c \approx 2.6$ mm, is about 82 mg. It remains unclear if these data are repeatable, or, if repeatable, the detailed mechanism of the transition process is still unclear.

In order to clarify the transition of relatively large drops depends on their sizes, careful experiments are reported here with two different methods of deposition of a droplet on the differently textured super-hydrophobic substrate. The experiments were conducted on super-hydrophobic surfaces consisting of arrays of 10 μm square posts, shown in Figure 2-1a. The silicon micro-post arrays were fabricated via standard photolithographic processes, followed by deep reactive ion etching. The substrates were further modified with a hydrophobic modifier, which is the trichloro(1H,1H,2H,2H-perfluorooctyl)silane by vapor phase deposition. The advancing contact angle, θ_a, of water on the fluorosilane coated smooth silicon was measured using a goniometer to be $120° \pm 3°$. The array of square posts produced super-hydrophobic surfaces whose capillary pressure $\Delta P_{cap,sqp}$ is given by

$$\Delta P_{cap,sqp} = \frac{4\gamma|\cos\theta_a|}{a[(1+b/a)^2 - 1]} \tag{2.3}$$

where γ is the surface tension of water, θ_a is the advancing contact angle on a smooth surface, a is the square post width, and b is the edge-to-edge spacing between posts.

The experiments were performed with various droplet volumes using two deposition methods. The wetting transition was detected by a dramatic decrease in contact angle and an increase in droplet adhesion to the surface. The volume of droplets was controlled with an automatic dispensing system.

In the first method, to approximate a quasi-static deposition, droplets were deposited onto surfaces with post spacings ranging from 40 to 75 μm using a small diameter stainless steel needle so as to minimize the drop adhesion to the needle. After forming a stable pendant droplet in the Cassie-Baxter state on the textured substrate, its volume was increased

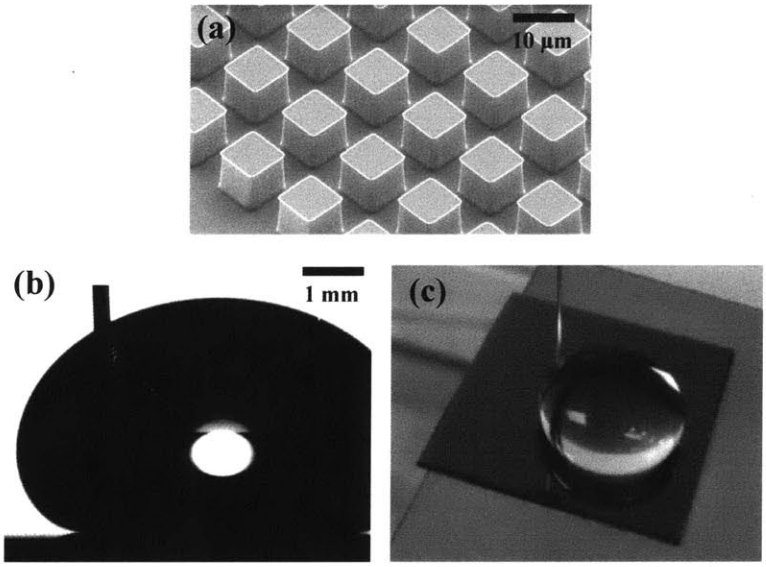

Figure 2-1: (a) SEM (scanning electron microscope) image of the 10 μm tall 10 μm by 10 μm square post array surface. (b) A 150 μL Cassie-Baxter droplet on a 75 μm spacing substrate and (c) a 500 μL Cassie-Baxter droplet on a 40 μm spacing substrate, as quasi-statically increased from a 5 μL CB droplet. The edge of the square substrate is 2 cm.

at a rate of 0.2 μL per second. The needle was not detached from the droplet. As the volume of these droplets increased, the transition into the Wenzel state was not observed even as the droplet volumes surpassed 500 μL (500 mg). The droplet seen in Figure 2-1b, c provides unambiguous evidence that a gravity-based transition is not observed even for droplets much larger than the critical mass of 82 mg, where gravitational and surface tension forces are of the same order for water. Obviously, in this experiment, the transition inducing pressure is the hydrostatic pressure that is insufficient even though the volume increases. This is because the height of a drop can be approximately the capillary length at most because of the surface tension. A drop cannot maintain its spherical shape, rather becoming a puddle. This result confirms that the gravity cannot solely cause the transition from Cassie-Baxter to Wenzel state.

The second method is based on careful deposition from a pendant droplet on the surface. To obtain a sessile droplet, it is necessary to detach a pendant droplet from the dispensing needle. The droplet deforms due to the surface tension forces at the tip of a needle, which scale with the diameter of a needle. Different diameter needles were selected so that pendant droplets would detach at volumes ranging from 7 μL to 90 μL. After forming a pendant droplet that is slightly smaller than the detachment volume, the droplet was lowered as close to the substrate as possible to be detached by further addition of volume, necking at the top of the droplet and subsequent detachment onto the substrate. The substrates with different post spacings (edge-to-edge), ranging from 40 μm to 100 μm, were used in the experiments.

As shown in Figure 2-2, it is apparent that large droplets are in the Cassie-Baxter state on 40 μm spaced posts; even with the volumes of 75 μL, the droplet remains in the Cassie-Baxter state. Only when a droplet was evaporated below its critical Laplace transition volume, which is 0.03 μL, a Wenzel droplet was observed on the 40 μm spaced square post substrate. The post array with the spacings between 60 to 87.5 μm exhibited a volume-dependent transition behavior. For example, on the 75 μm spaced substrate shown in Figure 2-2, the Wenzel state was observed for 1 μL droplets, no transition for 11 μL or 55 μL droplets, but the 75 μL droplet transitioned to the Wenzel state. On the 100 μm spaced substrate, all different size droplets, ranging from 7 μL to 75 μL, underwent transi-

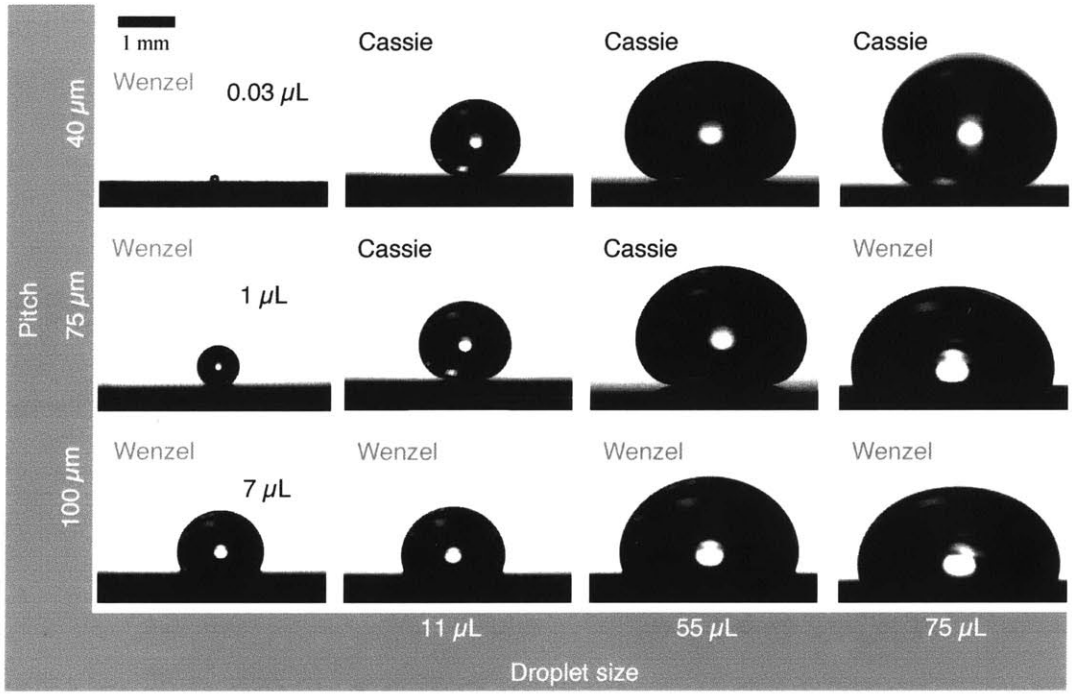

Figure 2-2: Stable sessile droplets with volumes from 0.03 μL to 75 μL deposited on the textured hydrophobic surfaces which are 10 μm tall 10 μm by 10 μm square post arrays with varying spacings. The Laplace pressure appears to cause transition of 0.03 μL and 1 μL droplets on the 40 μm and 75 μm spaced post arrays, respectively.

tion. Although the pendant droplets remained in the Cassie-Baxter state when brought into contact with the 100 μm spaced post array substrate, they became the Wenzel state upon detachment from the needle. These experimental observations show that the Cassie-Baxter to Wenzel transition can occur not only for small droplets by previously reported Laplace mechanism but also for large droplets.

To further understand the transition of large droplets, the deposition of a pendant droplets was recorded by the high-speed camera. The image sequence for the deposition of a 75 μL drop on the 75 μm spaced substrate is shown in Figure 2-3. It is seen that as the droplet settles initially on the substrate, there are surface perturbations and shape changes. A dominant feature is that the center of gravity of the droplet gets lowered by a length scale

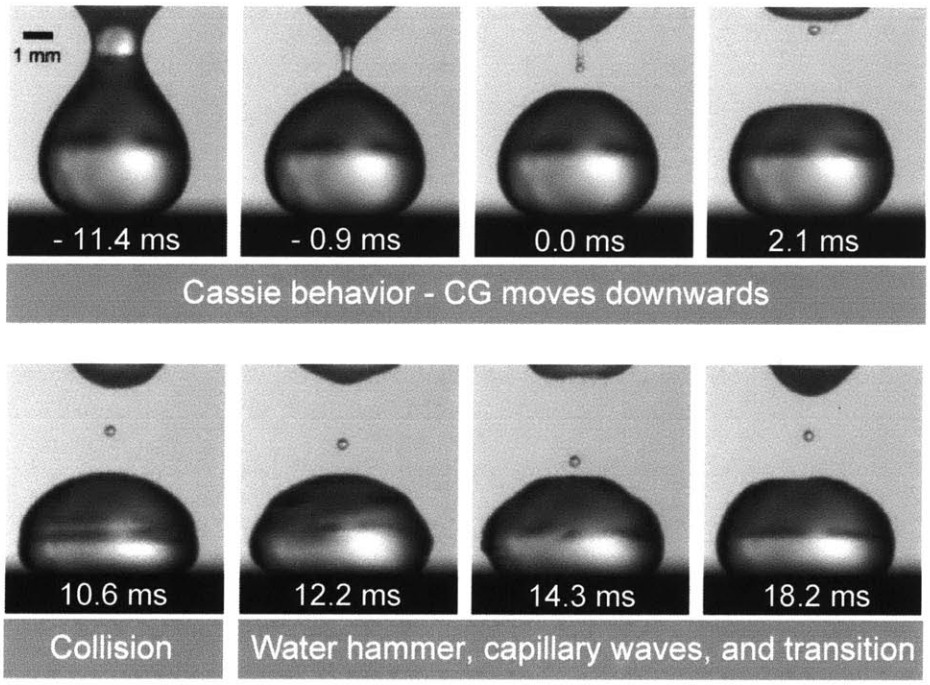

Figure 2-3: High-speed image sequence of 75 μL droplet detachment and wetting transition on the 75 μm spacing post array substrate during a careful droplet deposition from a pendant drop. The transition event occurs between 10.6 ms and 12.2 ms. The time scale of the center of the gravity motion of the droplet corresponds to the free fall time scale followed by capillary waves and transition.

$\Delta \sim 1\text{mm}$ on a time scale $t_{fall} \sim 10\text{ms}$ that corresponds to the free fall time scale, which is $\Delta \sim gt_{fall}^2$. This motion of the center of gravity gives rise to a velocity V_{fall}, estimated as

$$V_{fall} = \sqrt{2g\Delta} \tag{2.4}$$

With the given velocity, the corresponding dynamic pressure is

$$\Delta P_{dyn} = \frac{1}{2}\rho V_{fall}^2, \tag{2.5}$$

which is calculated here to be on the order of 10 Pa. The anti-wetting capillary pressure, $\Delta P_{cap,sqp}$, calculated for 75 μm spacing using Equation 2.3, is 202 Pa and far exceeds the dynamic pressure of 10 Pa. Therefore, the dynamic pressure is insufficient to induce the transition of the droplet to the Wenzel state. The high-speed image sequence in Figure 2-3 shows that the center of gravity of the drop stops moving down, representing a possible virtual collision with the substrate, in a very short time scale, which is less than the time resolution of the high speed camera. The transition to the Wenzel state occurs during this time, and is followed by a sudden evolution of capillary waves. It has been proposed that during this rapid deceleration, the pressure induced by this sudden deceleration can surge in an infinitesimal period of time, known as water hammer pressure [14] that is given as

$$\Delta P_{wh} = k\rho V_{fall} c \tag{2.6}$$

where k is a constant depending on the type of collision, shape, and velocity of the droplet [15] and c is the speed of sound. For the current case with low velocity and large droplet size, it has been found that $k = 0.001$ based on the experimental results. This implies ΔP_{wh} =2000 Pa, which is significantly larger than the anti-wetting capillary pressure for the given 75 μm spaced post array substrate, thereby causing the transition. Thus, the energy can be channeled by rapid deceleration into a large water hammer pressure that can result in transition to the Wenzel state.

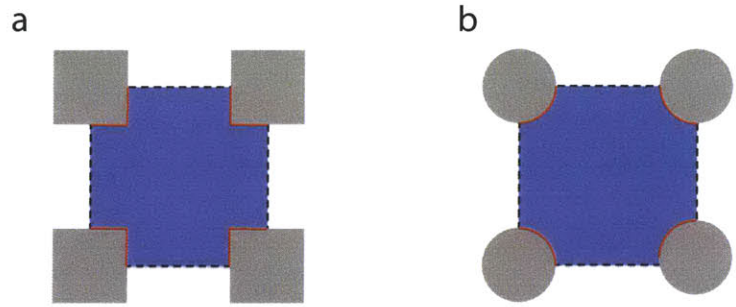

Figure 2-4: Schematics showing the definitions for the solid-liquid contact perimeter p (red line) and the projected area A of the meniscus (blue region) for unit cells of different post shapes (gray). Two common shapes are shown: (a) square and (b) circle.

2.3 Regime map of wetting states for different sizes of droplets

With the proposed mechanisms, the critical droplet sizes that transition from Cassie-Baxter to Wenzel state can be estimated. The three possible transition-inducing pressure terms discussed in the previous sections, the Laplace pressure, the dynamic pressure, and the water hammer pressure. The critical sizes of droplets that is to transition can be estimated by considering these three different pressures, and the regime map of the Cassie-Baxter state to the Wenzel state can be built for the different micro scale surface structures in an array form.

First, the maximum possible capillary pressure, given in Eq. 2.3, can be generalized for arrays of posts with other prismatic cross-sections in terms of the contact line perimeter p and the liquid-vapor interfacial area A projected onto a horizontal surface in a unit cell. In Figure 2-4, two examples of unit cells, a square post array (Figure 2-4a), and a circular post array (Figure 2-4b). As the liquid-air interface impales by an infinitesimal distance, denoted by dy in the following expression, the energy associated with the wetting is to be

balanced by the work done by the capillary pressure across the interface, which is expressed as

$$\Delta P_{cap,post} A dy = \gamma p |\cos\theta_a| dy \tag{2.7}$$

Rearrangement of the Eq.2.7 leads to

$$\Delta P_{cap,post} = \gamma p |\cos\theta_a| / A = \gamma / \ell_r \tag{2.8}$$

where ℓ_r defined in Eq. 2.8 is the length scale associated with the average radius of curvature of the liquid meniscus required to impale the roughness. For the square post array, the average radius of curvature is $\ell_r = 2b(1 + b/a)/(4|\cos\theta_a|)$.

The critical size of the droplets that can undergo Cassie-Baxter to Wenzel transition can be estimated from the velocity that arises from the free fall motion of the center of gravity. The displacement Δ can be estimated by considering the reduction in potential energy and the eventual gain in surface energy [16] as $\Delta \sim \rho g R^3/\gamma$ where R is the radius of the droplet. As the volume of the droplet increases, so do Δ and V_{fall}, given in Equation 2.4. Thus, the larger the droplets have the bigger transition inducing pressure, such as the dynamic pressure, ΔP_{dyn}, and the water hammer pressure, ΔP_{wh}.

The critical droplet radii corresponding to the different designs of micro textures can be estimated by equating the resisting capillary pressure, Equation 2.8, to the transition inducing pressures. For the sudden deceleration induced transition, it is the water hammer pressure, Equation 2.6. Then, the transition criteria is defined as

$$\frac{R^*_{wh}}{\ell_r} = \frac{1}{k^{2/3}} \left(\frac{\ell_c}{\ell_k}\right)^{1/3} \left(\frac{\ell_c}{\ell_r}\right)^{5/3} \tag{2.9}$$

where $\ell_k = 2c^2/g$ is a length scale based on the balance between sound wave and gravitational energies. Similar expressions for critical droplet radii R^*_d, and R^*_L, based on the dynamic and Laplace pressures, respectively, are

$$\frac{R^*_{dyn}}{\ell_r} = \left(\frac{\ell_c}{\ell_r}\right)^{4/3} \tag{2.10}$$

$$\frac{R^*_{lap}}{\ell_r} = 2 \tag{2.11}$$

According to the above mechanisms, the transition to the Wenzel state occurs if the radius of a droplet R is larger than R^*_{wh} or R^*_{den} and if R is smaller than R^*_{lap}. It is noted that the critical radius for the Laplace pressure driven transition, R^*_{lap}, is independent of the capillary length ℓ_c, implying that the gravity plays an insignificant role because the droplets are assumed to be smaller than the capillary length, ℓ_c. As $b/a \to 0$, $R^*_{lap} \sim b/|\cos\theta_a|$, which is the Laplace pressure induced transition according to the de-pinning mechanism. As b/a becomes large, $R^*_{lap} \sim b^2/(2a|\cos\theta_a|) \sim b^2/a$, which is the Laplace pressure driven transition according to the sag mechanism when the post height, $h \sim a$. Thus, the Equation 2.11 captures both the de-pinning and sag based transitions in their respective limits.

Equation 2.9, 2.10, 2.11 show that the capillary length scale becomes relevant for the water hammer driven or dynamic pressure driven transitions. Figuer 2-5 shows that the data are explained by the water hammer-based mechanism of transition.

In Figure 2-5, the critical droplet radii determined by each of three different pressures and the experimental results are plotted with the corresponding non-dimensionalized average radius of curvature $\chi = \ell_r/\ell_\gamma$. The estimated critical radii for the Laplace pressure induced transition and the water hammer pressure induced transition agree well with the experimental data, confirming that large droplets undergo transition due to the rapid deceleration induced water hammer pressure. The region between Laplace and water hammer transition lines represents the Cassie-Baxter regime while the outside area represents the Wenzel regime. Furthermore, it is worth of noting that the water hammer pressure based critical radius R^*_{wh} and Laplace-based critical radius R^*_{lap} intersect when

$$\chi_{crit} = \left(\frac{\ell_r}{\ell_c}\right)_{crit} = \left(\frac{\ell_c}{8\ell_k}\right)^{1/5} \tag{2.12}$$

Hence, any hydrophobic textures with $\chi \geq \chi_{crit}$ always have sessile droplets in the Wenzel state, such as the 100 μm spaced square posts in the experiments. Thus, it is seen that both large and small droplets transition to the Wenzel states due to the deceleration

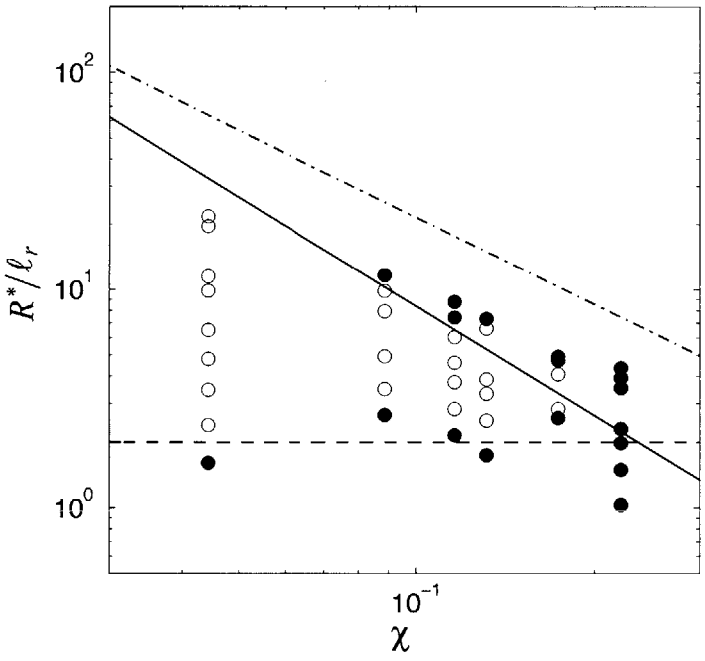

Figure 2-5: Size-dependent regime map of sessile droplets in the Cassie-Baxter state and the Wenzel states on textured hydrophobic surfaces. Predictions for normalized critical radius R^*/ℓ_r, of water droplets that undergo Cassie-Baxter to Wenzel transition as a function of the surface parameter based on different wetting pressures: water hammer pressure (solid), Laplace pressure (dashed), and dynamic pressure (dash-dot). The region between the Laplace and water hammer curves represents Cassie-Baxter regime while other regions represent the Wenzel regime. The experimental data are plotted as circles and consist of normalized droplet radii that are in Cassie-Baxter (open circles) and Wenzel (filled circles) states.

and the Laplace pressure of a droplet, respectively. These two transition criteria complete the regime map of droplet sizes in the Cassie-Baxter state and the Wenzel state as shown in Figure 2-5

Chapter 3

Increasing Leidenfrost temperature with super-wetting surface

Cooling of hot surfaces by impinging liquid drops is a widespread process in various fields such as emergency cooling of nuclear fuel rods under transient and accidental conditions, fire suppression, cooling of electronic and photonic devices, quenching processes in metallurgy, etc. Through this process, most of the heat is transferred to the liquid droplets as they directly contact solid surfaces. However, when the temperature of a solid is above the Leidenfrost point, liquid droplets levitate and no longer contact the surface due to the formation of a stable vapor layer [3]. The vapor layer acts as a thermal barrier, significantly limiting the heat transfer from the hot solid to the liquid coolant [52]. Under such conditions cooling becomes ineffective, causing the temperature of a substrate to reach dangerous levels, which results in local hotspots or catastrophic failures such as complete meltdown of a system, as is known to have occurred at the Fukushima disaster [53] Hence, higher Leidenfrost point is desirable for enhancing the cooling of overheated components.

The Leidenfrost phenomenon has received much attention in recent years in the context of non-wetting applications [54, 55], including the self-propulsion of liquid droplets [56] and solids[57], drag reduction [58], droplet impact [59], and liquid vitrification[60]. However, as discussed, increasing the Leidenfrost point is beneficial for cooling applications. Prior studies have shown that the Leidenfrost point can be raised by modifying the properties of liquids [61, 62, 63, 64, 65] and solids [66, 67, 68], and more recently by the

use of an electric field [69]. Modifying the surface is particularly attractive because liquid properties and other operational conditions are often constrained. Previous studies have identified surface roughness as an important property that generally leads to an increase in Leidenfrost point. Although promising, these studies have been limited to random roughness substrates such as, porous ceramics [70, 71], particle blasted and rough sanded [72], salt deposited [73], and particle coated [67]. As a result, the effects of surface texture on Leidenfrost point are not easily quantifiable, and the physical mechanisms governing the phenomenon remain largely unclear. Here, systematic experiments are carried out, which show that surface texture does not always increase Leidenfrost point. This study reveals a more complex picture where competition between texture-induced capillary pressures and dewetting vapor pressures influences the transition to the Leidenfrost state, and provide novel insights for increasing Leidenfrost point effectively using hierarchical textures.

3.1 Leidenfrost droplets on textured surfaces

The effect of surface texture on the Leidenfrost point is investigated by gently depositing millimetric droplets (30 μL, deionized water) onto heated silicon surfaces textured with arrays of microscale silicon square posts, shown in Figure 3-1. The post surfaces are fabricated using standard lithography techniques with post width a =10 μL, height h =10 μm and edge-to-edge spacing b ranging from 3.3 μm to 100 μm. For comparison, a smooth silicon surface without texture is also studied. All of the surfaces are subjected to Piranha cleaning [74] such that water droplets completely spread on the surfaces at room temperature (contact angle $\sim 0°$). The Leidenfrost point is determined by increasing the surface temperature in small increments and observing droplets transition from vigorous boiling to Leidenfrost state using a high-speed camera. For the smooth silicon surface the Leidenfrost point is found to be between 270°C at which a drop vigorously boils, and 300°C at which a drop floats on the surface, as shown in Figure 3-1a, and consistent with previous studies [67].

Interestingly, on textured surfaces the Leidenfrost point was found to be higher on surfaces with sparser rather than denser post spacings. For example, the Leidenfrost point on a

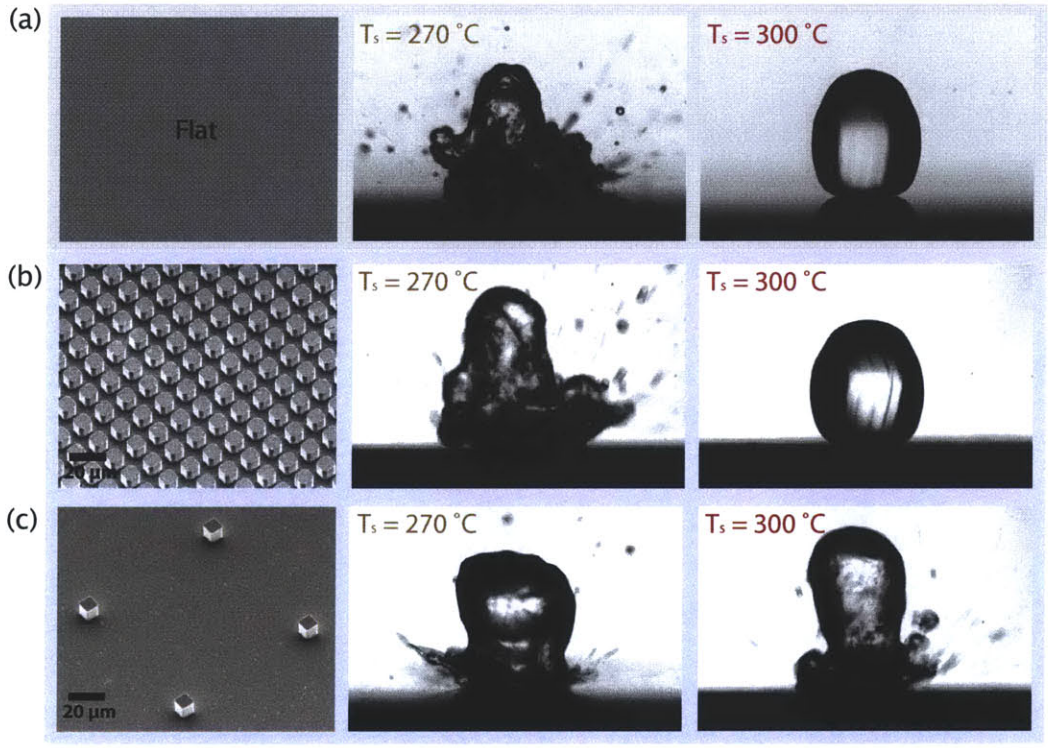

Figure 3-1: Effects of surface texture on drop dynamics at two different surface temperatures, T_s. (a) At $T_s = 270°\mathrm{C}$ (left), a deionized water drop spreads on the surface, and at the same time vigorously boils, ejecting smaller drops. At $T_s = 300°\mathrm{C}$ (right), a water drop floats on the surface without experiencing significant phase change, known as the Leidenfrost effect. The Leidenfrost transition temperature lies between 270°C and 300°C. (b), (c) Liquid droplets on micropost arrays (a =10 μm, h = 10 μm) with spacings b = 10 μm and b =75 μm, respectively, at the same two temperatures. The Leidenfrost point hardly changes with the dense post array, while the sparse post array promotes boiling by preventing the Leidenfrost effect.

textured surface with post spacing $b = 10$ μm was similar to that on a non-textured surface (Figure. 3-1b). However, when the post spacing was increased to $b = 75$ μm, the drop boils at both 270°C and 300°C (Figure 3-1c), indicating that the Leidenfrost point is higher on the sparser textures. Careful measurements of the transition from contact to floating states are presented in 3-2 where closed symbols depict contact and boiling, while open symbols depict flotation and Leidenfrost state. The Leidenfrost point is therefore the transition temperature between the two regimes. Inspection of Figure 3-2 indicates that as the post array becomes denser ($b \to 0$), the Leidenfrost point of a textured surface approaches that of a flat surface. As the array becomes sparser (as b increases), the Leidenfrost point increases, reaching a value of ~ 370°C for a spacing of $b = 100$ μm. This result is surprising because it would be commonly thought that denser textures should result in higher Leidenfrost point as they can facilitate enhanced wetting due to higher capillary forces [1].

3.2 Modeling of Leidenfrost droplets on textured surfaces

To rationalize these experimental findings, the following model is proposed. A drop that is in contact with the textured surface must detach if it is to float on its own vapor. It has been hypothesized that while the drop is in contact with the surface, it is subject to two competing processes, schematically described in Figure 3-3a, b. Specifically, capillary forces from the textured surface act to maintain contact by pulling the interface downwards while compressive forces from the vapor generated by the drop push the interface upwards. If these two competing mechanisms dominate the dynamics, then the drop will transition from wetting to floating when the force pushing it upward is comparable to the force pulling it downward. Using the schematic in Figure 3-3a, b as a guide, these competing forces can be estimated.

In the experiments drops gently impact the solid with a velocity ≈ 0.05 m/s ($We \sim 1$) to capture the role of the texture solely, keeping the inertia of drops as low as possible; however, even this gentle deposition can cause impalement into the micropost array [75]. The micropost array is hot enough that some of the impaled liquid quickly evaporates, creating a liquid-vapor interface. Because the solid surface is intrinsically highly wetting

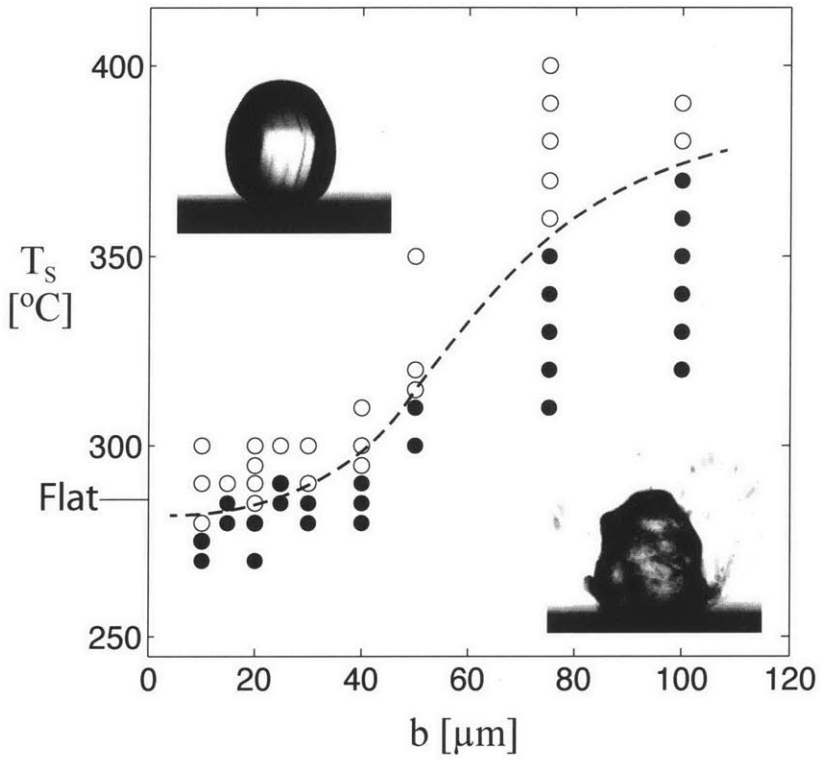

Figure 3-2: Experimental results of wetting and non-wetting drops from the micropost arrays with different spacings. Wetted boiling drops are denoted as closed circle markers, and a non-wetting Leidenfrost drops as open circle markers. The dashed line is only for visual clarity.

(*i.e.*, intrinsic contact angle $\sim 0°$), the liquid that is in contact with the surface is expected to form menisci as shown in Figure 3-3a, b. The characteristic curvature of the interface leads to a capillary pressure,

$$\Delta P_{cap} = \frac{\gamma}{b} \tag{3.1}$$

where γ is the surface tension between the liquid and the vapor. The capillary pressure leads to a force that pulls the interface downwards into the micropost array; the strength of this capillary adhesion increases as the spacing between the posts b decreases.

There is a competing force pushing up on the drop due to the compressive pressure from the vapor under the drop. As the drop evaporates, the vapor under the drop pressurizes to the point where it can drive an outward flow. The surface texture hinders this outward vapor flow and therefore to achieve the same flow rate in the presence of texture requires a larger pressure differential. The pressure under the drop can be estimated by modeling the vapor flow as a viscous-dominated radial Poiseuille flow [54, 70]. There are two components of shear losses to the flow: one in the vertical direction and one in the horizontal direction [76]. The vertical component scales as $\mu_v V/e^2$ where μ_v is the dynamic viscosity, V is the velocity of vapor, and e is the thickness of the vapor layer. The horizontal component scales as $\mu_v V/b^2$ where b is the post spacing. Therefore, the combined pressure gradient across the vapor flow in the radial direction dP_{vap}/dr scales as

$$\frac{dP_{cap}}{dr} \sim \mu_v V \left(\frac{1}{e^2} + \frac{1}{h^2} \right) \tag{3.2}$$

By introducing K, the approximate permeability,

$$K = \left(\frac{1}{e^2} + \frac{1}{h^2} \right)^{-1} \tag{3.3}$$

, The Equation 3.2 becomes

$$\frac{dP_{cap}}{dr} \sim \mu_v \frac{V}{K} \tag{3.4}$$

Because the flow rate is generated from evaporation, the value of V can be approximated with an energy balance [54]. The vapor mass flow rate $dm_{vap}/dt \sim \rho_v V e$ is balanced with the evaporation from the total amount of heat transferred through the gap

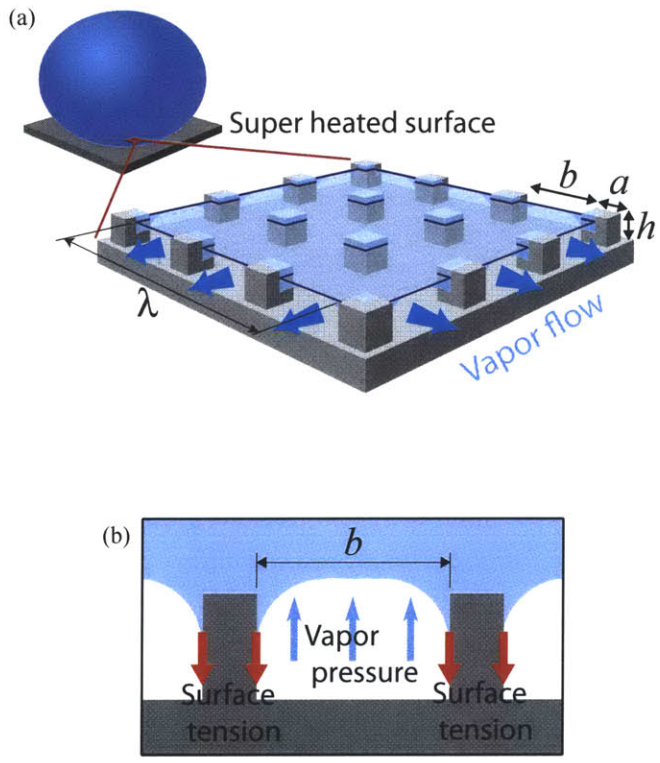

Figure 3-3: Schematic representation of the liquid interface on a textured surface at an elevated temperature. (a) As liquid comes into contact with the surface, it spreads out through hydrophilic solid features while rapidly evaporating at the interface due to super heat from the solid. The vapor starts to find paths to escape and the posts resist the flow resulting in a pressure differential. (b) Finally, continuous re-wetting through the surface features is possible when the capillary pressure overcomes the pressure from the flowing vapor.

$dm_{eval}/dt \sim q\lambda/h_{fg}$ where ρ_v is the vapor density, q is the heat flux, h_{fg} is the latent heat of vaporization, and λ is the length of the contact patch that is in contact with the surface. Therefore, the force per area pushing upward on the drop under a contact patch of length λ scales as

$$\Delta P_{vap} \sim \frac{\mu_v q \lambda^2}{\rho_v h_{fg} e K} \tag{3.5}$$

. The conductive heat flux q from the hot surface can be expressed as

$$q = k_{eff} \frac{\Delta T}{e} \tag{3.6}$$

. where ΔT is the temperature difference between the substrate temperature T_s and the vapor saturation temperature T_{sat}. The effective thermal conductivity k_{eft} can be related to the micropost geometry by approximating the parallel solid and vapor thermal paths between the drop and the substrate, which is

$$k_{eff} = k_v \frac{(1 + b/a)^2 - 1}{(1 + b/a)^2} + ks \frac{1}{(1 + b/a)^2} \tag{3.7}$$

where k_v is the thermal conductivity of vapor, and k_s is the thermal conductivity of the surface texture.

3.3 Prediction of the Leidenfrost transition of droplets on textured surfaces

In the model, the transition to the Leidenfrost state occurs when the pressure exerted by the flowing vapor overcomes the texture-induced capillary pressure. At this transition point the thickness of the vapor is approximately equal to the height of the microposts, $e \approx h$. It has been observed that the interface near transition is composed of numerous dynamic pinning and depinning regions under the drop [67]. These perturbations lead to capillary waves throughout the drop and ejection of small satellite droplets. The size of these droplets is comparable to the wavelength of these perturbations and thus comparable to the length of the local contact patch. The size of these droplets near Leidenfrost point were measured,

and it has been found that the diameter is approximately 60 μm. Therefore, the critical contact patch length at transition in the physical model is approximated as $\lambda^* \sim 60\ \mu$m, as indicated in Figure 3-3a.

The physical model predicts that the transition to the Leidenfrost state occurs when the vapor pressure at the transition moment, ΔP^*_{gap} is balanced by the capillary pressure, ΔP_{cap},

$$\frac{\Delta P^*_{vap}}{\Delta P_{cap}} \sim 1 \tag{3.8}$$

For the heated, micropost array, this pressure balance can be expressed in terms of the texture spacing as

$$\frac{\Delta P^*_{vap}}{\Delta P_{cap}} \sim \frac{\mu_v k_{eff} \Delta T^* \lambda^{*2} b}{\rho_v h_{fg} h^2 K \gamma} \tag{3.9}$$

where ΔT^* is the difference between the substrate temperature at the Leidenfrost point, T_{LFP} and the vapor saturation temperature, T_{sat}. The values of this ratio is calculated with the experimentally measured transition temperatures for different micropost arrays, shown in Figure 3-2 and indeed find that $\Delta P^*/\Delta P_{cap}$ is of order one as plotted in Figure 3-4. A slight dependence with b is observed in Figure 3-4, which may indicate that one of the parameters, modeled as constant, such as λ^*, might also depend on the spacing b. Nevertheless, the overall result that the two pressures are comparable at transition is consistent with the physical model and highlights the dual role of texture. It appears that textures elevates the Leidenfrost point by increasing capillary pressure, but also limits the Leidenfrost point elevation by increasing the resistance to the escaping vapor flow.

3.4 Effective hierarchical textures to increase the Leidenfrost point

If the physical model presented here is correct, it would follow that further elevation of the LFP might be possible if the texture could increase the capillary pressure without increasing the resistance to the escaping vapor flow. This prediction inspired us to develop a hierarchical textured surface, which is fabricated by spin-coating nanoparticles (220 nm diameter silica particles) onto an etched micropost array ($b = 75\ \mu$m). When comparing

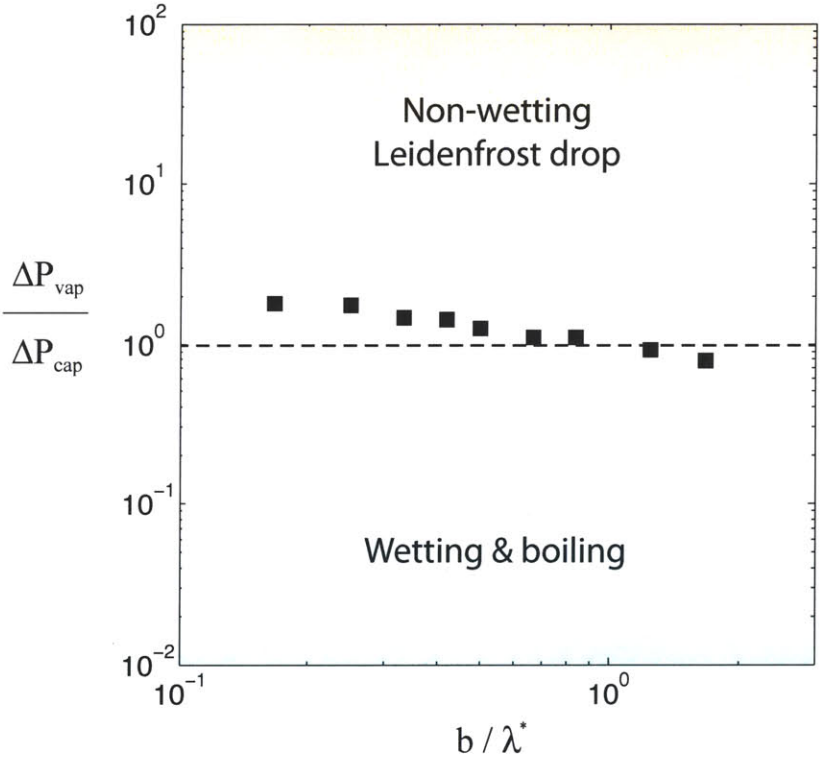

Figure 3-4: Vapor pressure normalized by capillary pressure for the experimentally measured Leidenfrost points, marked as the closed squares, for each different texture, corresponding to the post spacing normalized by the critical contact length, b/λ^*. The experiments show reasonable matches to the line where the capillary wetting pressure balances the draining vapor pressure, The transition to the Leidenfrost state happens when the vapor pressure overcomes the capillary pressure.

the performance of the hierarchical surface at a temperature above the Leidenfrost point for the non-hierarchical control surfaces, the results, shown in Figure 3-5 are striking. When the substrates are at 400°C (the limit of the current experimental setup), an impacting drop will float above both a surface with a single micro-scale texture ($b = 75$ μm; Figure 3-5a) and a surface with a single nano-scale texture ($b = 800$ nm; Figure 3-5b). However, when a drop impacts the micro-nano hierarchical surface texture heated to the same temperature, the drop rapidly wets the surface demonstrating that the Leidenfrost point has been significantly elevated (Figure 3-5c). All three results are consistent with the mechanisms in the physical model when the wetting depends on the smallest texture lengthscale and vapor resistance depends on the largest texture lengthscale. Other factors may also contribute to this effect, such as nucleation site density increment, and local compressibility that may change the escaping vapor pressure and the vaporization temperature of a liquid. Nevertheless, the experimental results and physical model provide insight into how surface texture design can have a profound effect on the Leidenfrost point.

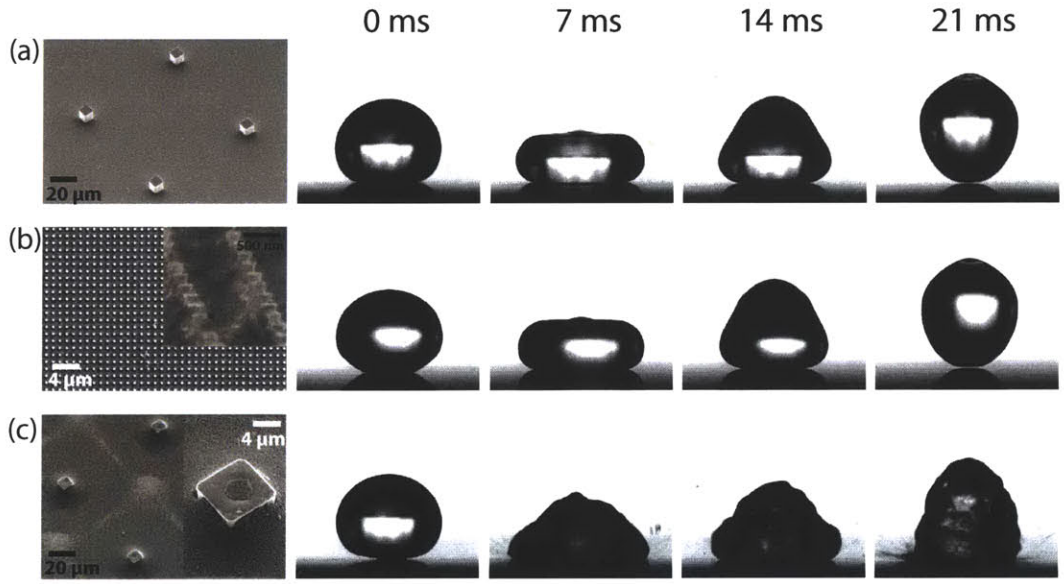

Figure 3-5: High speed image sequences of liquid drop behaviors on 400°C surfaces with three different surface textures: (a), (b) are single-length scale texture while (c) is a hierarchical texture. (a). microscale texture, 10 μm by 10 μm posts, with 75 μm spacing (b) nano scale texture, 200 nm diameter circular pillar array with 800 nm spacing. (c) Micro-nano hierarchical surface texture, with 10 μm by 10 μm posts array with 75 μm spacing, covered with nano-particles (avg. 220 nm diameter). The hierarchical texture unlike those in (a) and (b) promotes droplet wetting and boiling at 400°C.

Chapter 4

Textured superhydrophobic rare-earth oxide surface by laser ablation

As covered through the previous chapters, suitably textured hydrophobic surfaces achieve super-hydrophobicity, and the fabrication of super-hydrophobic surfaces has been extensively studied [19, 77, 78]. Recently, its promising potential for enhancing energy efficiency of existing systems in broad industrial applications has been more repeatedly highlighted, including drag reduction [79, 80], anti-icing [81, 24, 82], and drop-wise condensation [83, 84, 85]. In order to be applied widely for actual industrial processes, the textured super-hydrophobic surfaces have to be robust in harsh environments [78]. However, the robustness of these surfaces still remains a question. One of the reasons is that many textured super-hydrophobic surfaces inevitably rely on a hydrophobic modifier [86]. Most of the modifiers are polymers that readily deteriorate under extreme conditions. Although it has been shown that some super-hydrophobic surfaces have been created by directly texturing hydrophobic solids [87, 88, 89], the accessible hydrophobic solids are limited to mostly polymeric materials. Common durable industrial materials, such as metals and ceramics, are generally hydrophilic. Therefore, the interest naturally turns to hydrophobic metals or ceramics, a recently discovered hydrophobic rare-earth oxide series with the potential for realizing durable hydrophobic surfaces [4]. These rare-earth oxide ceramics sustained their intrinsic hydrophobicity under harsh conditions, such as high temperature, abrasive wear, and steam. As a result, the durable super-hydrophobic surfaces can

be realized as hydrophobic rare-earth oxides incorporate proper micro/nano-scale surface textures. For example, super-hydrophobic surfaces can be fabricated by coating conventionally made micro- and nano-scale hierarchical textures with a thin film of hydrophobic rare-earth ceramics [4]. Another way to create super-hydrophobic ceramics is to directly texture the hydrophobic ceramics. One of the simplest ways to create micro-/nano-scale surface structures for industrial materials, such as metals and ceramics, is laser modification [90, 91, 92, 93, 94].

In this study, a textured super-hydrophobic cerium oxide surface is prepared by direct laser irradiation. The bulk pallet of ceria is hydrophobic, but it is difficult to produce micro/nano-sized surface textures on it because of its high degree of hardness and strong wear resistance [4]. However, a simple laser-ablation process with a nano-second Nd:YAG laser creates micro/nano hierarchical textures, which are favorable for the further enhancement of water-repellency from single scale textures. After the multiple times of 100 ns pulsed laser irradiations, the surface of the pellet has been textured with micro- and nano-scale hierarchical roughness, resulting in the super-hydrophobic surface. The hydrophobicity of the textured ceria has been characterized by measuring contact angles of a water drop on it. Its water repellency is demonstrated by observing that an impinging droplet completely bounces off this surface. Examining the X-ray photoelectron spectroscopy (XPS) data confirms that the surface chemistry remains the same as before the laser irradiation.

4.1 Hydrophobic rare-earth ceramics and laser induced textures

The ceria pellet was prepared first. It was fabricated from raw powders of ceria ($< 5\ \mu$m, 99.9 % from Sigma Aldrich) in the as-received conditions. The powders were dry-pressed in a cylindrical steel press mold into disk-shaped pellets (28.5 mm in diameter and $\sim$2 mm thick) first under a pressure of 270 MPa for 3 minutes, followed by a second round of pressing at 350 MPa for 5 minutes. The green body was then sintered in a dry air environment inside a tube furnace at 1560°C for 4 hours. To obtain surface morphology

and average grain size, the micro-structural characterization of the sintered pellets was performed using scanning electron microcopy, shown in Figure 4-1. It was shown that ceria pellet is densely sintered into a honeycomb structure with an average grain size of 15±5 μm. The relative density of the sintered ceria was measured in water using Archimedes principle [95] and found to be 99.4 % of its theoretical density, which is 7.21 g/cm^3 [4].

After sintering, the ceria pellet was polished to a mirror finish to minimize the effect of roughness on contact angle measurements. When it was polished, the sintered pellet had an advancing contact angle of 102±3°, shown in Figure 4-1, and a receding contact angle of 55±3°, measured with water droplets. Then, the surface of the ceria pellet was textured with laser irradiation, which was Nd:YAG laser (1064 nm wavelength, 150 W maximum continuous output, Electrox) at 20 kHz at 100 ns pulse in air. Each beam was shot in a square array at an approximately 13 μm distance for the entire pellet, and the same irradiation was repeated 20 times. After the laser process, the pellet was cleaned by rinsing with isopropyl alcohol, followed by ethanol and then acetone and finally extensive rinsing with deionized water for 5 minutes. Cleaned sample was dried by blowing nitrogen gas and kept in a desiccator under vacuum prior to contact angle measurements.

4.2 Water repellency of textured super-hydrophobic ceria

The textured ceria pellet has shown good water repellency. The water contact angle of the surface was measured as 160±5°, shown in Figure 4-1; thereby the contact angle hysteresis of 5° indicates increased water repellency from the smooth pellet whose contact angle hysteresis is 48°. The enhancement of the water repellency resulted from the micro- and nano-scale hierarchical textures that the multiple irradiation of laser created. The scanning electron microscopic images in Figure 4-1d show the hierarchical textures, self-organized under multiple irradiations of laser beams. The textures consist of 5 μm to 15 μm mudcrack like features, covered with around 50 nm to 100 nm sized protrusions. The formation of micro-size polygonal features could have evolved in an analogous way to mudcracks, which is formed by the strain, developed as the top part of muddy sediments shrinks while the bottom part stays the same. The localized laser irradiation melts a small area of the

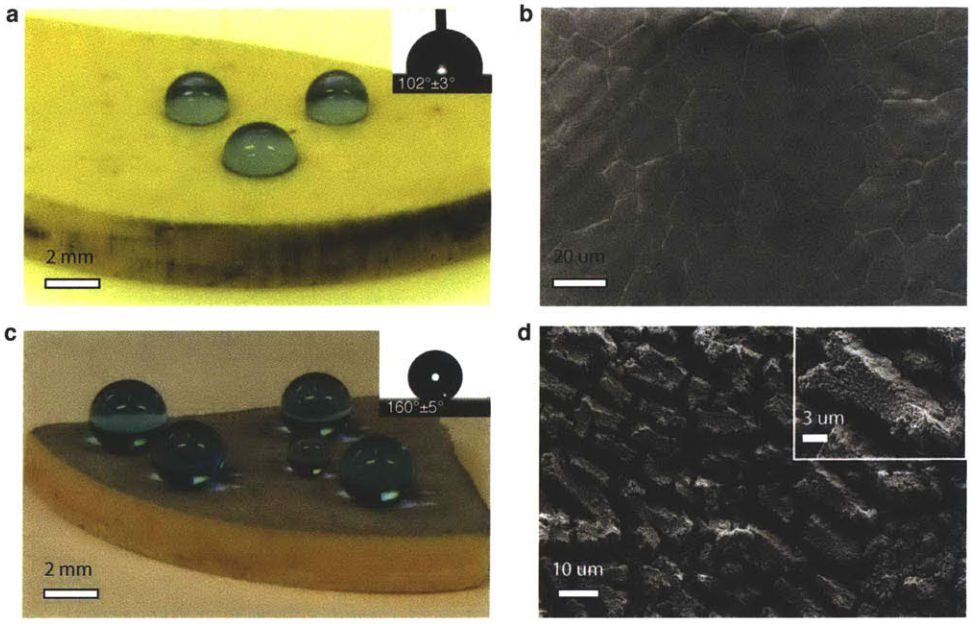

Figure 4-1: Superhydrophobicity of laser-ablated ceria sintered pellet. (a) Photograph of dyed water droplets on a sintered ceria pellet ($\theta = 102° \pm 3°$); scale bar 2.0 mm. (b) Scanning electronic micrograph of ceria (CeO_2) surface (average grain size: 15 ± 5 μm);; the scale bar is 20 μm. (c) Photograph of dyed water droplets on the laser ablated ceria pellet ($\theta = 160° \pm 5°$); the scale bar is 2.0 mm. (d) Scanning electronic micrograph of laser-ablated ceria sintered ceramic; the scale bar is 10 μm. The inset shows a high magnification SEM image (scale bar is 3 μm).

material, and evaporates some portion of it at the top; then as the material cools down, the cracks are formed on the surface. The nano-scale bumps are suspected of being created by the recrystallization of the melted parts as well as the precipitation of evaporated parts.

The enhanced water repellency is shown by a drop impact experiment. A deionized water drop whose radius is 2.5 mm with the velocity of 1.5 $\mathrm{m/s}$ impacts the laser textured ceria substrate, corresponding to the Weber number, $We \sim 78$. The drop impingement was captured by a high speed camera, and Figure 4-2 shows the sequential images of the experiment. The textured ceria surface was able to completely repel the impacting drop.

Figure 4-2: Water repellency of laser-ablated ceria sintered pellet. High-speed photography images of a water droplet bouncing off of the laser-ablated ceria sintered ceramic (impact velocity ~ 1.5 m/s); the scale bar is 2.5 mm.

4.3 Material characterization of the laser induced surface textures on ceria

To confirm the chemical composition at the surface after the laser ablation, the surface chemistry was examined by X-ray photoelectron spectroscopy (XPS). Figure 4-3a, and b show the XPS spectra of the ceria pellet before and after laser ablation, respectively. XPS analysis found Ce, O, and C at these surfaces. As shown in the spectra, the laser induced textured surface shows the similar chemical composition at the surface to the original ceria pellet. Before laser irradiation, the pellet consisted of around 30.5% Ce (Figure 4-3a) and this value remained almost unchanged after laser ablation (Figure 4-3a). The atomic percent of O and C before laser ablation were about 60.0% and 9.5%, respectively. After the laser ablation, a small variation in O and C concentration was observed: the concentration of O at the surface was reduced to 52.2% and C content was increased to about 16.4%. Such small variations can be due to the atmospheric contaminants that could have been introduced during sample handling in the laser ablation process. Therefore, the observed super-hydrophobicity on the laser-ablated ceria pellet is mainly due to the hierarchical structure that was introduced at the surface of the hydrophobic ceria pellet. In

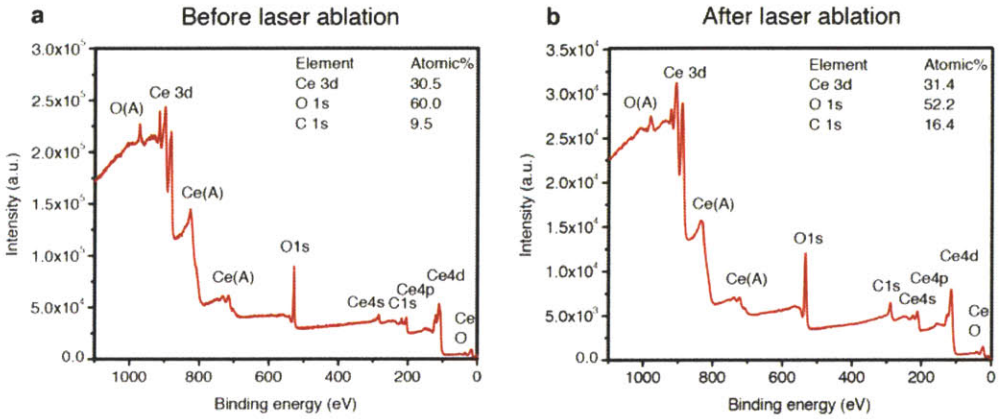

Figure 4-3: XPS spectra of the ceria pellet: (a) before and (b) after the laser ablation. The spectra verify that the surface chemistry remains unchanged after laser ablation process, and show that carbon contamination is negligible at the surface.

summary, one robust hydrophobic ceramic, ceria, has been textured with laser ablation, resulting in self-organized micro/nano two length scale hierarchical textures. The surface texturing by itself shows enhanced water repellency without a hydrophobic modifier, since the bulk ceria is hydrophobic, confirmed by the surface chemistry data from the current XPS examination.

Chapter 5

Conclusion

It has been explored how engineered surface textures can benefit the industrial processes by tailoring the hydrodynamics of the non-wetting droplets in different cases, one by the textured super-hydrophobic surfaces, and the other one by the vapor layer from a large superheat. In order to enhance the energy efficiency of those industrial processes, the interaction between liquid droplets and surfaces needs to be promoted or prevented. By identifying major roles of the surface textures on the hydrodynamics of droplets, the design parameters of the surface textures are understood, and it was possible to design the novel textures that enable more efficient energy transfer.

A rapid deceleration driven water hammer pressure can cause the transition from Cassie-Baxter to Wenzel droplets during deposition. A new phase diagram is presented where both small and large droplets can transition based on Laplace and water hammer mechanisms, respectively. This result implies that the Cassie-Baxter state can be achieved via pendant droplet deposition only for intermediate droplet sizes for many rough surfaces that are not optimally designed. This insight is novel and shows that the attainment of a Cassie-Baxter state is more restrictive than previously implied by Laplace pressure-based transition mechanism.

The following study has identified that Leidenfrost phenomenon on textured surfaces occurs when capillary pressures balance compressive pressures exerted by the vapor. The microscopic textures with sparser spacings are preferable to increase the Leidenfrost point. It has also been shown that the Leidenfrost point can be further increased by using hier-

archical textures. These insights can be used to enhance the heat transfer performance in various applications, including cooling of nuclear fuel rods under transient and accident conditions, fire suppression, electronics cooling, and quenching processes in metallurgy.

Additionally, the new hydrophobic materials and the fabrication methods are introduced, which ensure the robustness under harsh industrial conditions. The laser ablation of ceria results in self-organized micro/nano two length scale hierarchical textures. The surface texturing by itself shows enhanced water repellency without a hydrophobic modifier, since the bulk ceria is hydrophobic, confirmed by the surface chemistry from the XPS examination. The water repellency of the surface was demonstrated by the high degree of the contact angle, the lowered value of contact angle hysteresis, and the complete rebound of an impinging water droplet. This study extends the possibility of producing robust super-hydrophobic rare-earth oxide ceramics with the benefit of using easily accessible nano-second laser techniques for industrial applications.

Bibliography

[1] David Quéré. Wetting and roughness. *Annual Review of Materials Research*, 38(1):71–99, 2008.

[2] Denis Richard, Christophe Clanet, David Quéré, et al. Contact time of a bouncing drop. *Nature*, 417(6891):811, 2002.

[3] Johann Gottlob Leidenfrost. *De aquae communis nonnullis qualitatibus tractatus*. [Typis Joan. Sebast. Straube, Acad. typogr.] Impensis Hermanni Ovenni, Univers. bibliopolæ, 1756.

[4] Gisele Azimi, Rajeev Dhiman, Hyuk-Min Kwon, Adam T Paxson, and Kripa K Varanasi. Hydrophobicity of rare-earth oxide ceramics. *Nature Materials*, 12:315–320, 2013.

[5] ABD Cassie and S. Baxter. Wettability of porous surfaces. *Transactions of the Faraday Society*, 40:546–551, 1944.

[6] Robert N. Wenzel. Resistance of solid surfaces to wetting by water. *Industrial and Engineering Chemistry*, 28(8):988–994, 1936.

[7] Yong Chae Jung and Bharat Bhushan. Wetting transition of water droplets on superhydrophobic patterned surfaces. *Scripta Materialia*, 57(12):1057 – 1060, 2007.

[8] H. Kusumaatmaja, M. L. Blow, A. Dupuis, and J. M. Yeomans. The collapse transition on superhydrophobic surfaces. *EPL (Europhysics Letters)*, 81(3):36003, 2008.

[9] M. Reyssat, J. M. Yeomans, and D. Quéré. Impalement of fakir drops. *EPL (Europhysics Letters)*, 81(2):26006, 2008.

[10] N.A. Patankar. Consolidation of hydrophobic transition criteria by using an approximate energy minimization approach. *Langmuir*, 26(11):8941–8945, 2010.

[11] J.F Oliver, C Huh, and S.G Mason. Resistance to spreading of liquids by sharp edges. *Journal of Colloid and Interface Science*, 59(3):568 – 581, 1977.

[12] Neelesh A. Patankar. Transition between superhydrophobic states on rough surfaces. *Langmuir*, 20(17):7097–7102, 2004.

[13] Zen Yoshimitsu, Akira Nakajima, Toshiya Watanabe, and Kazuhito Hashimoto. Effects of surface structure on the hydrophobicity and sliding behavior of water droplets. *Langmuir*, 18(15):5818–5822, 2002.

[14] Tao Deng, Kripa K. Varanasi, Ming Hsu, Nitin Bhate, Chris Keimel, Judith Stein, and Margaret Blohm. Nonwetting of impinging droplets on textured surfaces. *Applied Physics Letters*, 94(13):133109, 2009.

[15] O.G. Engel. Waterdrop collisions with solid surfaces. *Journal of Research. National Bureau of Standards*, 5:281–298, 1955.

[16] L. Mahadevan and Yves Pomeau. Rolling droplets. *Physics of Fluids*, 11(9):2449–2453, 1999.

[17] Pierre-Gilles De Gennes, Françoise Brochard-Wyart, and David Quéré. *Capillarity and wetting phenomena: drops, bubbles, pearls, waves*. Springer, 2003.

[18] Xuefeng Gao and Lei Jiang. Biophysics: water-repellent legs of water striders. *Nature*, 432(7013):36–36, 2004.

[19] David Quéré. Non-sticking drops. *Reports on Progress in Physics*, 68(11):2495, 2005.

[20] Ralf Blossey et al. Self-cleaning surfaces-virtual realities. *Nature materials*, 2(5):301–306, 2003.

[21] Anish Tuteja, Wonjae Choi, Minglin Ma, Joseph M. Mabry, Sarah A. Mazzella, Gregory C. Rutledge, Gareth H. McKinley, and Robert E. Cohen. Designing superoleophobic surfaces. *Science*, 318(5856):1618–1622, 2007.

[22] Xu Deng, Lena Mammen, Hans-Jürgen Butt, and Doris Vollmer. Candle soot as a template for a transparent robust superamphiphobic coating. *Science*, 335(6064):67–70, 2012.

[23] Lidiya Mishchenko, Benjamin Hatton, Vaibhav Bahadur, J. Ashley Taylor, Tom Krupenkin, and Joanna Aizenberg. Design of ice-free nanostructured surfaces based on repulsion of impacting water droplets. *ACS Nano*, 4(12):7699–7707, 2010.

[24] Adam J. Meuler, Gareth H. McKinley, and Robert E. Cohen. Exploiting topographical texture to impart icephobicity. *ACS Nano*, 4(12):7048–7052, 2010.

[25] Stefan Jung, Manish K Tiwari, N Vuong Doan, and Dimos Poulikakos. Mechanism of supercooled droplet freezing on surfaces. *Nature Communications*, 3:615, 2012.

[26] S Chandra and CT Avedisian. On the collision of a droplet with a solid surface. *Proceedings: Mathematical and Physical Sciences*, pages 13–41, 1991.

[27] Christophe Clanet, Cédric Béguin, Denis Richard, David Quéré, et al. Maximal deformation of an impacting drop. *Journal of Fluid Mechanics*, 517:199–208, 2004.

[28] Martin Rein. Phenomena of liquid drop impact on solid and liquid surfaces. *Fluid Dynamics Research*, 12(2):61, 1993.

[29] Jens Eggers, Marco A. Fontelos, Christophe Josserand, and Stéphane Zaleski. Drop dynamics after impact on a solid wall: Theory and simulations. *Physics of Fluids*, 22(6):062101, 2010.

[30] D. Richard and D. Quéré. Bouncing water drops. *EPL (Europhysics Letters)*, 50(6):769, 2000.

[31] D. Bartolo, F. Bouamrirene, É. Verneuil, A. Buguin, P. Silberzan, and S. Moulinet. Bouncing or sticky droplets: Impalement transitions on superhydrophobic micropatterned surfaces. *EPL (Europhysics Letters)*, 74(2):299, 2006.

[32] Yongjoo Kwon, Neelesh Patankar, Junkyu Choi, and Junghoon Lee. Design of surface hierarchy for extreme hydrophobicity. *Langmuir*, 25(11):6129–6136, 2009.

[33] Vance Bergeron, Daniel Bonn, Jean Yves Martin, and Louis Vovelle. Controlling droplet deposition with polymer additives. *Nature*, 405(6788):772–775, 2000.

[34] Denis Bartolo, Christophe Josserand, and Daniel Bonn. Retraction dynamics of aqueous drops upon impact on non-wetting surfaces. *Journal of Fluid Mechanics*, 545:329–338, 11 2005.

[35] Mathilde Reyssat, Denis Richard, Christophe Clanet, and David Quere. Dynamical superhydrophobicity. *Faraday Discussions*, 146:19–33, 2010.

[36] Xiying Li, Xuehu Ma, and Zhong Lan. Dynamic behavior of the water droplet impact on a textured hydrophobic/superhydrophobic surface: The effect of the remaining liquid film arising on the pillars' tops on the contact time. *Langmuir*, 26(7):4831–4838, 2010. PMID: 20151667.

[37] K. Okumura, F. Chevy, D. Richard, D. Quéré, and C. Clanet. Water spring: A model for bouncing drops. *EPL (Europhysics Letters)*, 62(2):237, 2003.

[38] Andrew K. Dickerson, Peter G. Shankles, Nihar M. Madhavan, and David L. Hu. Mosquitoes survive raindrop collisions by virtue of their low mass. *Proceedings of the National Academy of Sciences*, 109(25):9822–9827, 2012.

[39] Ken C Cotton. *Evaluating and improving steam turbine performance*. Cotton Fact, 1998.

[40] Geoffrey Taylor and Geoffrey Taylor. The dynamics of thin sheets of fluid. iii. disintegration of fluid sheets. *Proceedings of the Royal Society of London. Series A. Mathematical and Physical Sciences*, 253(1274):313–321, 1959.

[41] F. E. C. Culick. Comments on a ruptured soap film. *Journal of Applied Physics*, 31(6):1128–1129, 1960.

[42] Lord Rayleigh. On the capillary phenomena of jets. *Proceedings of the Royal Society of London*, 29(196-199):71–97, 1879.

[43] L.H.J. Wachters and N.A.J. Westerling. The heat transfer from a hot wall to impinging water drops in the spheroidal state. *Chemical Engineering Science*, 21(11):1047 – 1056, 1966.

[44] Jinping Liu, Xintang Huang, Yuanyuan Li, K. M. Sulieman, Xiang He, and Fenglou Sun. Hierarchical nanostructures of cupric oxide on a copper substrate: controllable morphology and wettability. *Journal of Materials Chemistry*, 16:4427–4434, 2006.

[45] R. Kurz and K. Brun. Degradation in gas turbine systems. *Journal of Engineering for Gas Turbines and Power*, 123(1):70–77, 2001.

[46] Otakar Jonas and Lee Machemer. Steam turbine corrosion and deposits problems and solutions. In *Proceedings of the 37th Turbomachinery Symposium*, 2008.

[47] Otakar Jonas and Joyce M Mancini. Steam turbine problems and their field monitoring. *Materials performance*, 40(3):48–53, 2001.

[48] V Petr, M Kolovratnik, I Jiricek, and O Jonas. Experimental investigation of the effects of steam chemistry on droplet nucleation. *Moisture Nucleation in Steam Turbines*, 1997.

[49] Victor Manuel Ortega-Jimenez and Robert Dudley. Aerial shaking performance of wet anna's hummingbirds. *Journal of The Royal Society Interface*, 9(70):1093–1099, 2012.

[50] Christian C. Voigt, Karin Schneeberger, Silke L. Voigt-Heucke, and Daniel Lewanzik. Rain increases the energy cost of bat flight. *Biology Letters*, 7(5):793–795, 2011.

[51] B D L Fitt, H A McCartney, and P J Walklate. The role of rain in dispersal of pathogen inoculum. *Annual Review of Phytopathology*, 27(1):241–270, 1989.

[52] Van P Carey. *Liquid-vapor phase-change phenomena.* Hemisphere, New York, NY (United States), 1992.

[53] J Buongiorno, R Ballinger, M Driscoll, B Forget, C Forsberg, M Golay, M Kazimi, N Todreas, and J Yanch. Technical lessons learned from the fukushima-daichii accident and possible corrective actions for the nuclear industry: An initial evaluation, 2011.

[54] Anne-Laure Biance, Christophe Clanet, and David Quere. Leidenfrost drops. *Physics of Fluids*, 15(6):1632–1637, 2003.

[55] David Quéré. Leidenfrost dynamics. *Annual Review of Fluid Mechanics*, 45(1), 2012.

[56] H. Linke, B. J. Alemán, L. D. Melling, M. J. Taormina, M. J. Francis, C. C. Dow-Hygelund, V. Narayanan, R. P. Taylor, and A. Stout. Self-propelled leidenfrost droplets. *Physical Review Letters*, 96:154502, Apr 2006.

[57] Guillaume Lagubeau, Marie Le Merrer, Christophe Clanet, and David Quéré. Leidenfrost on a ratchet. *Nature Physics*, 7(5):395–398, 2011.

[58] Ivan U. Vakarelski, Jeremy O. Marston, Derek Y. C. Chan, and Sigurdur T. Thoroddsen. Drag reduction by leidenfrost vapor layers. *Physical Review Letters*, 106:214501, May 2011.

[59] Tuan Tran, Hendrik J. J. Staat, Andrea Prosperetti, Chao Sun, and Detlef Lohse. Drop impact on superheated surfaces. *Physical Review Letters*, 108:036101, Jan 2012.

[60] Young S. Song, Douglas Adler, Feng Xu, Emre Kayaalp, Aida Nureddin, Raymond M. Anchan, Richard L. Maas, and Utkan Demirci. Vitrification and levitation of a liquid droplet on liquid nitrogen. *Proceedings of the National Academy of Sciences*, 107(10):4596–4600, 2010.

[61] C.T. Avedisian and M. Fatehi. An experimental study of the leidenfrost evaporation characteristics of emulsified liquid droplets. *International Journal of Heat and Mass Transfer*, 31(8):1587 – 1603, 1988.

[62] Y. M. Qiao and S. Chandra. Experiments on adding a surfactant to water drops boiling on a hot surface. *Proceedings of the Royal Society of London. Series A: Mathematical, Physical and Engineering Sciences*, 453(1959):673–689, 1997.

[63] V. Bertola. Drop impact on a hot surface: effect of a polymer additive. *Experiments in Fluids*, 37:653–664, 2004.

[64] V. Bertola. An experimental study of bouncing leidenfrost drops: Comparison between newtonian and viscoelastic liquids. *International Journal of Heat and Mass Transfer*, 52(7â"8):1786 – 1793, 2009.

[65] Gail Duursma, Khellil Sefiane, and Aiden Kennedy. Experimental studies of nanofluid droplets in spray cooling. *Heat Transfer Engineering*, 30(13):1108–1120, 2009.

[66] JD Bernardin and Issam Mudawar. The leidenfrost point: experimental study and assessment of existing models. *Transactions-American Society Of Mechanical Engineers Journal Of Heat Transfer*, 121:894–903, 1999.

[67] Hyungdae Kim, Bao Truong, Jacopo Buongiorno, and Lin-Wen Hu. On the effect of surface roughness height, wettability, and nanoporosity on leidenfrost phenomena. *Applied Physics Letters*, 98(8):083121, 2011.

[68] Ivan U Vakarelski, Neelesh A Patankar, Jeremy O Marston, Derek YC Chan, and Sigurdur T Thoroddsen. Stabilization of leidenfrost vapour layer by textured superhydrophobic surfaces. *Nature*, 489(7415):274–277, 2012.

[69] Franck Celestini and Geoffroy Kirstetter. Effect of an electric field on a leidenfrost droplet. *Soft Matter*, 8:5992–5995, 2012.

[70] C.T. Avedisian and J. Koplik. Leidenfrost boiling of methanol droplets on hot porous/ceramic surfaces. *International Journal of Heat and Mass Transfer*, 30(2):379 – 393, 1987.

[71] S. Chandra and C.T. Avedisian. Observations of droplet impingement on a ceramic porous surface. *International Journal of Heat and Mass Transfer*, 35(10):2377 – 2388, 1992.

[72] John D Bernardin, Clinton J Stebbins, and Issam Mudawar. Effects of surface roughness on water droplet impact history and heat transfer regimes. *International Journal of Heat and Mass Transfer*, 40(1):73 – 88, 1996.

[73] Qiang Cui, Sanjeev Chandra, and Susan McCahan. The effect of dissolving salts in water sprays used for quenching a hot surface: Part 1—boiling of single droplets. *Journal of Heat Transfer*, 125(2):326–332, 03 2003.

[74] Stephen D Senturia. *Microsystem design*, volume 3. Kluwer academic publishers Boston, MA, 2001.

[75] Hyuk-Min Kwon, Adam T. Paxson, Kripa K. Varanasi, and Neelesh A. Patankar. Rapid deceleration-driven wetting transition during pendant drop deposition on superhydrophobic surfaces. *Physical Review Letters*, 106:036102, Jan 2011.

[76] C. Ishino, M. Reyssat, E. Reyssat, K. Okumura, and D. Quéré. Wicking within forests of micropillars. *EPL (Europhysics Letters)*, 79(5):56005, 2007.

[77] Paul Roach, Neil J. Shirtcliffe, and Michael I. Newton. Progess in superhydrophobic surface development. *Soft Matter*, 4:224–240, 2008.

[78] Lydéric Bocquet and Eric Lauga. A smooth future? *Nature Materials*, 10(5):334–337, 2011.

[79] Chang-Hwan Choi and Chang-Jin Kim. Large slip of aqueous liquid flow over a nanoengineered superhydrophobic surface. *Physical Review Letters*, 96:066001, Feb 2006.

[80] Bharat Bhushan and Yong Chae Jung. Natural and biomimetic artificial surfaces for superhydrophobicity, self-cleaning, low adhesion, and drag reduction. *Progress in Materials Science*, 56(1):1 – 108, 2011.

[81] Liangliang Cao, Andrew K. Jones, Vinod K. Sikka, Jianzhong Wu, and Di Gao. Anti-icing superhydrophobic coatings. *Langmuir*, 25(21):12444–12448, 2009. PMID: 19799464.

[82] Peng Guo, Yongmei Zheng, Mengxi Wen, Cheng Song, Yucai Lin, and Lei Jiang. Icephobic/anti-icing properties of micro/nanostructured surfaces. *Advanced Materials*, 24(19):2642–2648, 2012.

[83] Jonathan B. Boreyko and Chuan-Hua Chen. Self-propelled dropwise condensate on superhydrophobic surfaces. *Physical Review Letters*, 103:184501, Oct 2009.

[84] Kripa K. Varanasi, Ming Hsu, Nitin Bhate, Wensha Yang, and Tao Deng. Spatial control in the heterogeneous nucleation of water. *Applied Physics Letters*, 95(9):094101, 2009.

[85] Konrad Rykaczewski, John Henry J. Scott, Sukumar Rajauria, Jeff Chinn, Amy M. Chinn, and Wanda Jones. Three dimensional aspects of droplet coalescence during dropwise condensation on superhydrophobic surfaces. *Soft Matter*, 7:8749–8752, 2011.

[86] Tuukka Verho, Chris Bower, Piers Andrew, Sami Franssila, Olli Ikkala, and Robin H. A. Ras. Mechanically durable superhydrophobic surfaces. *Advanced Materials*, 23(5):673–678, 2011.

[87] Neil J Shirtcliffe, Sanaa Aqil, Carl Evans, Glen McHale, Michael I Newton, Carole C Perry, and Paul Roach. The use of high aspect ratio photoresist (su-8) for superhydrophobic pattern prototyping. *Journal of Micromechanics and Microengineering*, 14(10):1384, 2004.

[88] M.T. Khorasani, H. Mirzadeh, and Z. Kermani. Wettability of porous polydimethylsiloxane surface: morphology study. *Applied Surface Science*, 242(3â"4):339 – 345, 2005.

[89] R. Martijn Wagterveld, Christian W. J. Berendsen, Salim Bouaidat, and Jacques Jonsmann. Ultralow hysteresis superhydrophobic surfaces by excimer laser modification of su-8. *Langmuir*, 22(26):10904–10908, 2006.

[90] Izhak Etsion. State of the art in laser surface texturing. *Advanced Tribology*, pages 761–762, 2010.

[91] John F Ready, Dave F Farson, and Terry Feeley. *LIA handbook of laser materials processing*. Laser Institute of America Orlando, 2001.

[92] J. Lawrence, L. Li, and J.T. Spencer. Diode laser modification of ceramic material surface properties for improved wettability and adhesion. *Applied Surface Science*, 138-139(0):388 – 393, 1999.

[93] Barada K. Nayak and Mool C. Gupta. Self-organized micro/nano structures in metal surfaces by ultrafast laser irradiation. *Optics and Lasers in Engineering*, 48(10):940 – 949, 2010.

[94] K.-H. Zum Gahr and J. Schneider. Surface modification of ceramics for improved tribological properties. *Ceramics International*, 26(4):363 – 370, 2000.

[95] James A Jacobs and Thomas F Kilduff. *Engineering materials technology: structures, processing, properties, and selection*. Prentice hall, 1997.